



A wideband and high-gain circularly polarized reconfigurable antenna array based on the solid-state plasma

Lei Zhang, Qian-Qian Li, Hai-Feng Zhang^{*}

College of Electronic and Optical Engineering & College of Flexible Electronics (Future Technology), Nanjing University of Posts and Telecommunications, Nanjing 210023, China



ARTICLE INFO

Keywords:

Circularly polarized antenna
Solid-state plasma
Characteristic mode analysis
Polarization-reconfigurable antenna
Spoof surface plasmon polariton

ABSTRACT

In this paper, a wideband and high-gain circularly polarized (CP) antenna array with polarization-reconfigurable characteristics is presented based on the solid-state plasma (SSP). The proposed antenna is composed of switchable rotating radiation structures and a switchable feed network by simulating the different SSP branches. To investigate the CP operating mechanism, a reconfigurable CP element is designed through characteristic mode analysis (CMA). A switchable sequential-phase feed network is then proposed which can provide separately two rotational excitations. A spoof surface plasmon polariton (SSPP) is adopted for radiation patches to improve gain and axial ratio (AR) bandwidth. Finally, a high-gain and wideband 2×2 CP reconfigurable antenna array is designed. This array achieves left-hand circular polarization (LHCP) and right-hand circular polarization (RHCP) modes when different SSP branches are excited. The array has an overlapped impedance bandwidth of 61.9 % (3.17 to 6.01 GHz) and an overlapped AR bandwidth of 40.2 % (4.01 to 6.03 GHz) in two CP states, and the peak gain is 11.68 dBi.

1. Introduction

Recently, antennas with reconfigurable characteristics have received increasing attention in modern wireless communication systems. Of particular interest are circularly polarized (CP) reconfigurable antennas capable of generating both left-hand circular polarization (LHCP) and right-hand circular polarization (RHCP) radiations. Such antennas are highly convenient in communication systems such as GNSS, WLAN, and mobile satellite communication. They can effectively mitigate multipath fading losses, improve system capacity, and enhance link quality [1–3]. It is both meaningful and challenging to design a reconfigurable CP antenna with high gain, wide bandwidth, and compact dimensions.

There are two essential techniques frequently utilized in the creation of CP reconfigurable antennas: the implementation of reconfigurable radiation components [4–7] and the utilization of reconfigurable feed networks [8–11]. However, antennas employing both methods tend to exhibit a shared drawback i.e., narrow bandwidths and inadequate gain. A reconfigurable Wilkinson power divider was fabricated in Ref. [12], capable of producing 0° and 90° phase differences. Feeding the antenna with this network can switch the polarization states between linearly polarized (LP) mode, LHCP mode, and RHCP mode. Nonetheless, its

overlapped bandwidth is only 13.1 % and the peak gain is 9 dBi. In Ref. [13], a compact microstrip-slot line-CPW feed network has been reported to design a 2×2 polarization reconfigurable antenna array operating at S-band. However, the axial ratio (AR) bandwidth of this design is limited to only 14.5 %, presenting a formidable challenge in increasing the AR bandwidth of CP reconfigurable antennas. To overcome this limitation, various methods have been proposed. In Ref. [3], a tuning resistor is introduced on the annular slot to significantly increase the AR bandwidth by approximately 27.9 %. In Ref. [5], by introducing a differentially-fed, L-shaped dipole as a perturbation to separate the degenerate modes, wideband CP radiation could be realized. A switchable cross-bowtie radiator is proposed to achieve wideband CP reconfigurability [14], whose AR bandwidth is 21.7 %. In Ref. [15], Metasurfaces acting as parasitic elements can also enhance the AR bandwidth to 25.6 %.

However, these technologies have limited bandwidth improvement for antennas and may increase the size. To further enhance the performance of the antenna, the proposed design in this paper incorporates spoof surface plasmon polariton (SSPP) technology. SSPP have generated significant interest in the microwave community. These are electromagnetic (EM) excitations that propagate along corrugated metal

* Corresponding author.

E-mail address: hanlor@njupt.edu.cn (H.-F. Zhang).

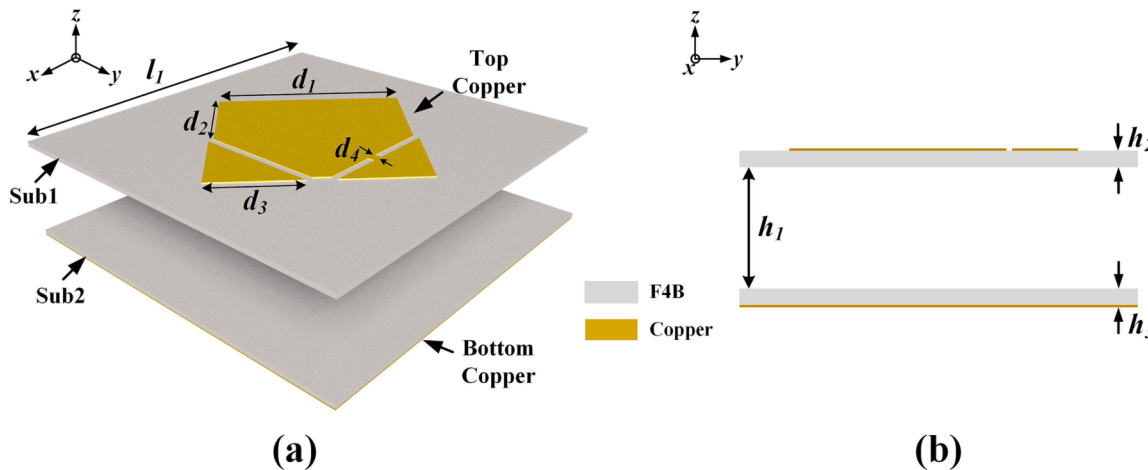


Fig. 1. Configuration of the proposed antenna element: (a) Schematic view, (b) Side view.

surfaces and exhibit characteristics that are similar to real surface plasmon polariton occurring at optical frequencies [16,17]. When periodic metal structures are employed, transversal magnetic surface waves can be sustained and effectively guided. The whole structure exerts an influence that reduces the plasma resonance frequency of the metal, enabling the achievement of this frequency band in microwave frequencies. Numerous antennas have achieved high gain through the introduction of SSPP [18–23]. The tight confinement of EM waves around the metal surface is a key benefit of SSPP.

Additionally, many 2×2 arrays have recently been proposed to generate broadband CP radiation using the sequential-phase feed technique, including microstrip antennas [24–26], dipole antennas [27,28], and monopole antennas [29,30]. Although originally an LP element or a CP element with a limited bandwidth, a substantial CP bandwidth can be generated by exciting elements with appropriate sequential rotation and phase differences. The feeding network adopted direct 1-to-4 power dividers [24,25]. However, the feeding network utilized Wilkinson power dividers, 90° phase shifters, and 180° phase shifters to devise ultra-wideband CP antennas [26–30]. In Ref. [30], the feeding network employed three cascaded Wilkinson power dividers to further enhance the antenna bandwidth.

In addition to the aforementioned methods, characteristic mode analysis (CMA) has also been widely employed to physically understand the antenna working principle. CMA is an appropriate method for examining the operating mechanism of antennas, primarily by investigating the current distribution of characteristic modes and analyzing the radiating behavior [31–37]. In Ref. [32], CMA is performed on a hexagon-shaped slotted patch to comprehend the concept of circularly polarized radiation. In Ref. [34], CMA is utilized to design an antenna that achieves wide bandwidth, compact size, stable pattern, and low cross-polarization. A wideband and high-isolated back-cover antenna pair for smartphones is designed by employing two sets of characteristic modes in Ref. [36]. In brief, CMA confers notable advantages in terms of improving the accuracy of antenna design.

Positive-intrinsic negative (PIN) diodes and varactor diodes are commonly used to reconfigure the radiation aperture or peripheral bias circuit of an antenna, enabling reconfigurability of the antenna's operating state. For PIN diodes, the operating frequency can be changed to meet specific requirements, but continuous scanning of the operating frequency is limited. On the other hand, varactor diodes provide an excellent solution for continuous frequency scanning; however, the low self-resonant frequency of commercial varactor diodes restricts their tunable frequency range. Additionally, micro-electro-mechanical system (MEMS) switches [38,39] and tunable materials are also available for reconfigurable antennas. Among these options, the use of tunable materials can serve as flexible radio frequency (RF) switches to alter the

antenna structure [40]. For example, gaseous plasma, due to its high conductivity in the ionized state, can replace the metal parts of the antenna to enable beamforming and resonant frequency transformation. However, the large size, high power consumption, and difficulties in the mass production of gaseous plasma formation devices limit their practicality. Solid-state plasma (SSP) antennas, a type of plasma antenna, utilize semiconductor and silicon processing technologies for the fabrication of high-performance, high-yield transverse PIN devices [41]. By applying an external bias voltage, the SSP region exhibits metal-like characteristics, thus altering the antenna's performance [42,43]. Compared to traditional reconfigurable antennas, SSP antennas offer advantages such as flexible operating frequency band switching, wide radiation direction range, and good stealth characteristics. As a result, they have become a popular research topic worldwide for achieving antenna miniaturization and enhancing wireless communication system performance [44].

This paper focuses on a wideband, high-gain CP reconfigurable antenna. The antenna can switch between LHCP and RHCP by manipulating different SSP branches. Here, CMA is applied to provide more insights into the antenna operation. The element with excellent CP radiation performance at 4.87 GHz is first designed. A reconfigurable sequential-phase feed network has been designed based on the conventional Wilkinson power divider capable of exciting LHCP and RHCP. SSPP is introduced to localize the energy, resulting in a 2.5 dBic increase in peak gain. These components are successfully combined with the feed network to realize a wideband and high-gain CP reconfigurable antenna with an overlapped bandwidth of 40.2 % from 4.01 to 6.03 GHz, and it also has a peak gain of 11.68 dBic.

2. Design of CP element

In this section, a concise exposition of the theory of CMA is presented initially, followed by a thorough investigation of the inherent circular polarization principle of the element informed by the CMA.

2.1. Characteristic mode theory

CMA is a technique that can visually describe the series of mutually orthogonal and convergent characteristic modes of arbitrarily shaped conductors without any excitation [32]. The characteristic modes are a completely orthogonal set utilized to extend all the corresponding currents and excitation far-fields induced by specific excitation sources. In other words, the induced current on a perfect electric conductor (PEC) can be represented as the superposition of characteristic currents, defined as Eq. (1) [36].

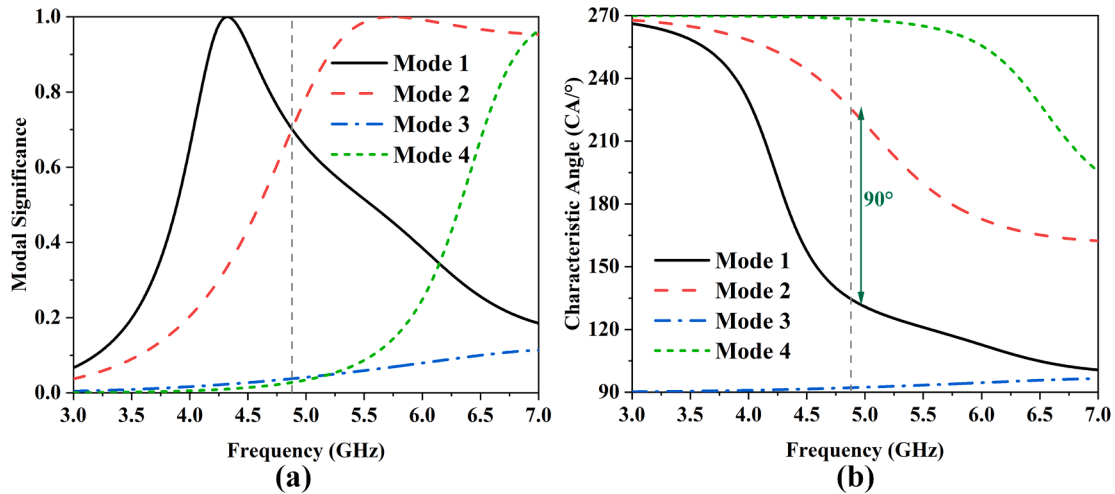


Fig. 2. (a) MS and (b) CA for the first four modes of the proposed antenna element.

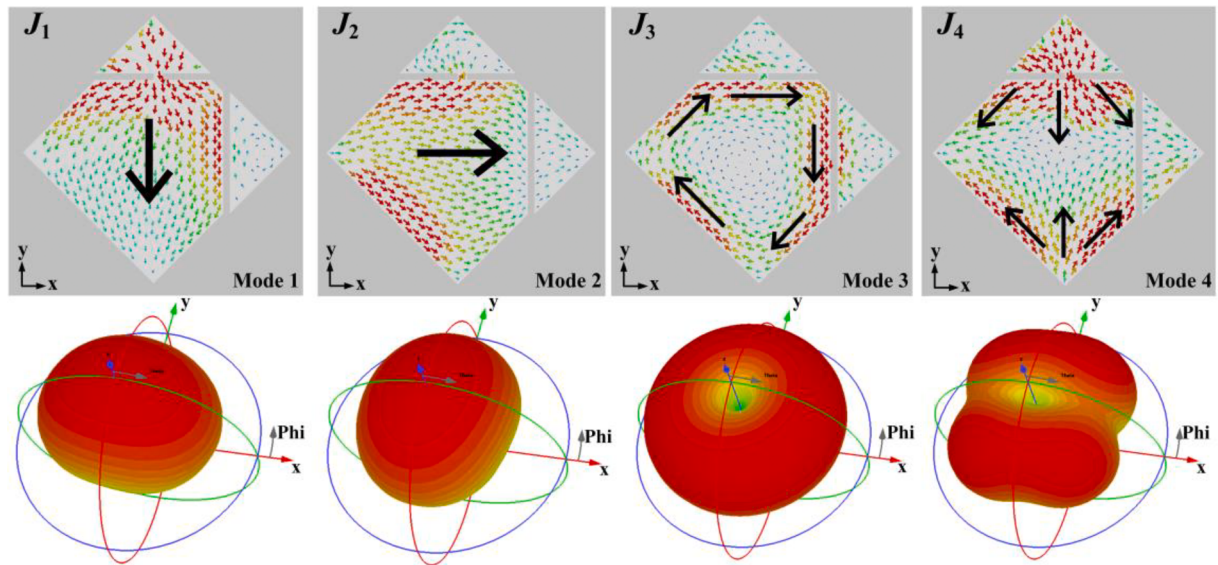


Fig. 3. Modal currents and radiation patterns of mode 1-mode 4 at 4.87 GHz.

$$\mathbf{J} = \sum_{n=1}^N C_n \cdot \mathbf{J}_n \quad (1)$$

where \mathbf{J}_n is the characteristic current of mode n and C_n refers to the complex modal weighting coefficient (MWC) to be determined for each mode. The mode significance (MS) is an intrinsic property of the mode that is independent of any externally applied excitation sources. It represents the coupling ability between the characteristic mode and internal sources, defined as Eq. (2) [35].

$$MS_n = \frac{1}{|1 + j\lambda n|} \quad (2)$$

MS and MEC together measure the contribution of each mode in a given excitation source to the total EM field. As evidenced by (2), the value of MS changes between 0 and 1. Furthermore, in practical antenna simulation analysis, a characteristic mode can be considered a resonant mode if $MS > 0.7$ [33].

The characteristic mode theory defines a series of characteristic currents on the PEC body. These currents generate a characteristic electric field in free space. There exists a fixed phase difference between the tangential component of the characteristic current and the charac-

teristic electric field, which is referred to as the characteristic angle (CA), defined as Eq. (3) [35].

$$CA_n = 180^\circ - \tan^{-1}(\lambda n) \quad (3)$$

Circular polarization can be achieved by simultaneously exciting a pair of orthogonal modes. The two modes should meet the following requirements: (1) MS of the two modes should be quite close and able to achieve the resonance requirements. ($MS_1 = MS_2$), (2) there should be a 90° difference between the CAs, with $CA_1 = 135^\circ$ and $CA_2 = 225^\circ$, (3) the characteristic current directions of the two modes should be orthogonal to each other, and (4) the maximum radiation direction in the far-field pattern should be consistent.

2.2. CP element design based on CMA

A schematic and side view of the proposed CP antenna element is shown in Fig. 1. The antenna element is composed of top and bottom copper layers, printed on Substrate 1 and Substrate 2. The substrates are F4B with a relative permittivity of 2.2, a loss tangent of 0.003, and a size of $l_1 \times l_1$. It is noteworthy that the radiation patch of the antenna has undergone an evolution from a standard monopole design by

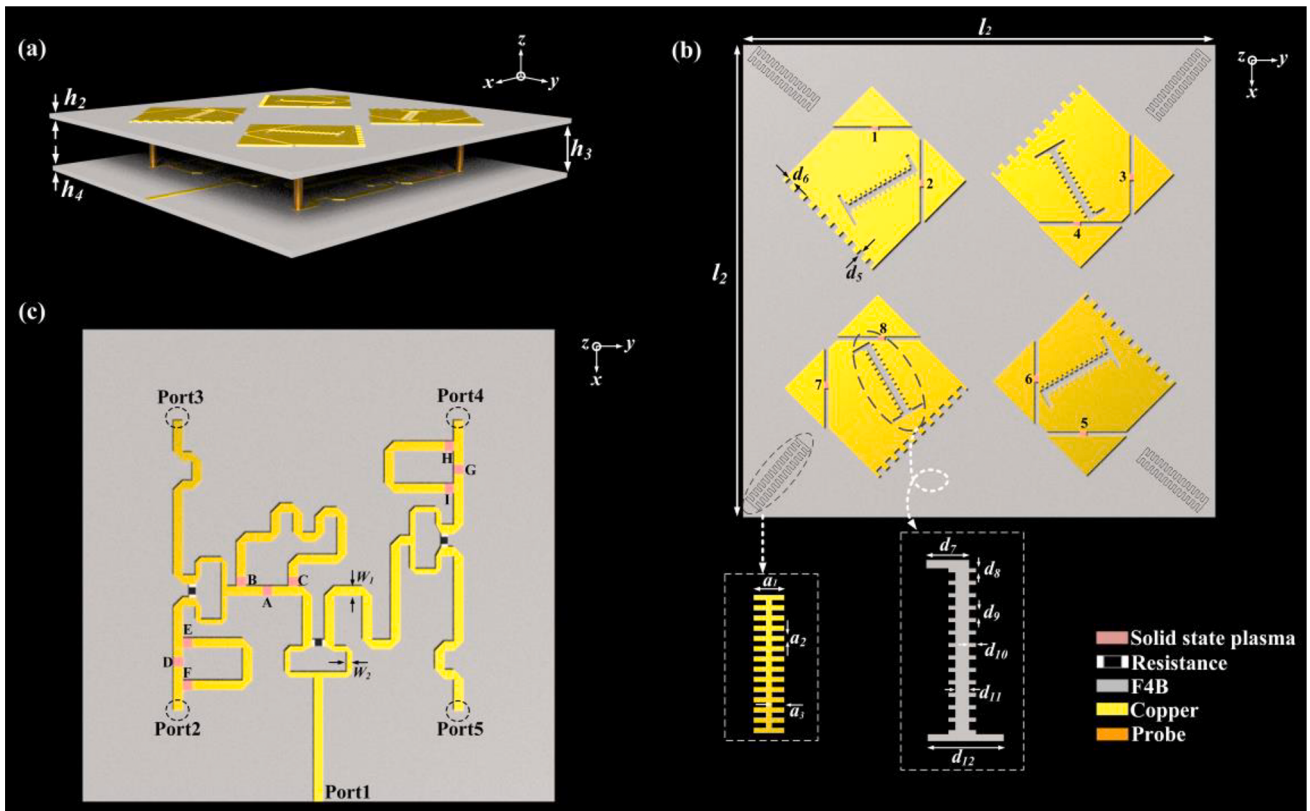


Fig. 4. Structure diagram of the antenna: (a) Schematic view, (b) Top view, (c) Feed network.

introducing two chamfered triangles, and one of which is connected to the remaining polygonal shape. The detailed parameters are as follows: $l_1 = 40 \text{ mm}$, $d_1 = 20 \text{ mm}$, $d_2 = 10.7 \text{ mm}$, $d_3 = 9.3 \text{ mm}$, $d_4 = 0.7 \text{ mm}$, $h_1 = 9 \text{ mm}$, $h_2 = 0.5 \text{ mm}$, and $h_3 = 0.5 \text{ mm}$.

For a comprehensive understanding of CP implementation of the CP element, CMA is applied to meticulously analyze the intrinsic modes of this element at various frequencies. The MS and CA of the first four modes mode 1-mode 4 are shown in Fig. 2. As can be observed in Fig. 2(a), both mode 1 and mode 2 exhibit a modal significance of 0.7 at 4.87 GHz, thus suggesting the possibility of exciting the first two modes jointly at this frequency. Fig. 2(b) further reveals a 90° difference between the characteristic angles of these two modes at 4.87 GHz. Therefore, simultaneous excitation of mode 1 and mode 2 leads to the emission of CP radiation.

In order to further analyze the CP radiation characteristics of the metal patch, modal currents and radiation patterns of the first four modes (mode 1-mode 4) at 4.87 GHz are presented in Fig. 3. It is remarkable that the modal current J_1 is linearly polarized in the y -axis direction, whereas the modal current J_2 is linearly polarized in the x -axis direction. As both two modes share the same MS value, mode 1 and mode 2 are a pair of degenerate modes. Moreover, modal current J_3 exhibits a clockwise rotation, while modal current J_4 is symmetric to the x -axis. Mode 1 and mode 2 exhibit similarity in their radiation patterns owing to their orthogonality and degeneracy, with mutually perpendicular polarization. In contrast, mode 3 and mode 4, being of higher order, are considered irrelevant. Therefore, a pair of orthogonal radiation fields, characterized by identical amplitudes and a phase difference of 90°, can be generated through the simultaneous excitation of mode 1 and mode 2. As a result, the antenna achieves CP radiation at 4.87 GHz.

3. 2 × 2 CP reconfigurable antenna array

3.1. Array configuration

It is well known that the excitation of the antenna element with a suitable sequential phase difference can produce an appreciable CP bandwidth. A 2 × 2 CP reconfigurable antenna array is further designed based on the CP antenna element. Fig. 4 shows the geometry of the proposed reconfigurable antenna array, with an overall size of $1.0\lambda \times 1.0\lambda \times 0.09\lambda$ (where λ is the wavelength in free space at the lowest operating frequency).

Fig. 4(a) is the schematic view of the antenna array. The antenna array is a double-layer structure with a sequential-phase feed network feeding the radiation patches through four metallic probes. Fig. 4(b) is a top view of the CP reconfigurable antenna array. The left and right rotational switching of the radiation patch is achieved by exciting SSP branches (1–8) so that they correspond to the phase of the four ports in the reconfigurable feed network. SSPP is introduced to improve the gain and bandwidth, periodic jagged slots are excavated into the radiation patch, while notches are etched around the smooth metal. Four additional serrated metal shapes are printed at the corners of the lower surface. Fig. 4(c) shows a schematic of the reconfigurable feed network, where the input signal can be equally distributed through the Wilkinson power divider. To make the four ports of the feed network have the characteristics of left or right rotation switching, nine SSP branches (A-I) are introduced to make it reconfigurable. The detailed parameters are as follows: $l_2 = 75 \text{ mm}$, $d_5 = 1 \text{ mm}$, $d_6 = 1.1 \text{ mm}$, $d_7 = 3.1 \text{ mm}$, $d_8 = 0.4 \text{ mm}$, $d_9 = 0.6 \text{ mm}$, $d_{10} = 0.5 \text{ mm}$, $d_{11} = 1 \text{ mm}$, $d_{12} = 5.5 \text{ mm}$, $a_1 = 3$, $a_2 = 0.5 \text{ mm}$, $a_3 = 1.2 \text{ mm}$, $h_4 = 6 \text{ mm}$.

The SSP of the proposed antenna is generated by the transverse structure of silicon-based PIN units. As the bias voltage increases, the carrier concentration within the entire region increases. When it reaches approximately 2 V, the carrier concentration in the entire region reaches 10^{18} cm^{-3} , and the plasma exhibits sufficient conductivity [45]. At this

Table 1
Antenna reconfigurability.

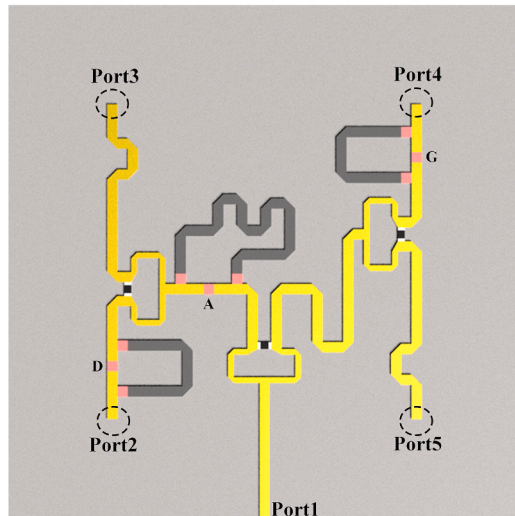
Polarization	The excited SSP branches	Not excited SSP branches
LHCP	1, 3, 5, 7, A, D, and G	2, 4, 6, 8, B, C, E, F, H, and I
RHCP	2, 4, 6, 8, B, C, E, F, H, and I	1, 3, 5, 7, A, D, and G

point, the entire region exhibits metallic-like characteristics and is in a conductive state; otherwise, it displays dielectric characteristics and is in a cutoff state. The increase in carrier concentration upon excitation

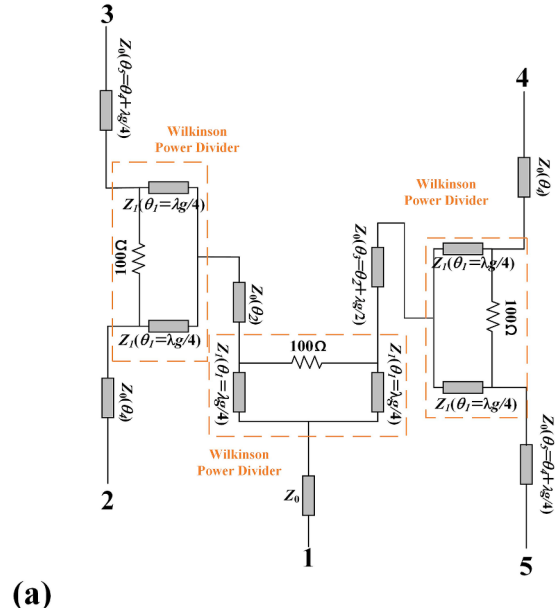
further affects the plasma frequency ω_p and the collision frequency ω_c , as shown in Eqs. (4) and (5). Therefore, the frequency-dependent permittivity of the SSP can be described by the Drude model in Eq. (6) [46,47].

$$\omega_p = \sqrt{\frac{e^2 n_e}{\epsilon_0 m_e}} \quad (4)$$

$$\omega_c = 1.7 \times 10^{11} \frac{mn}{2.7 \times 10^{19}} \sqrt{\frac{T}{300}} \quad (5)$$

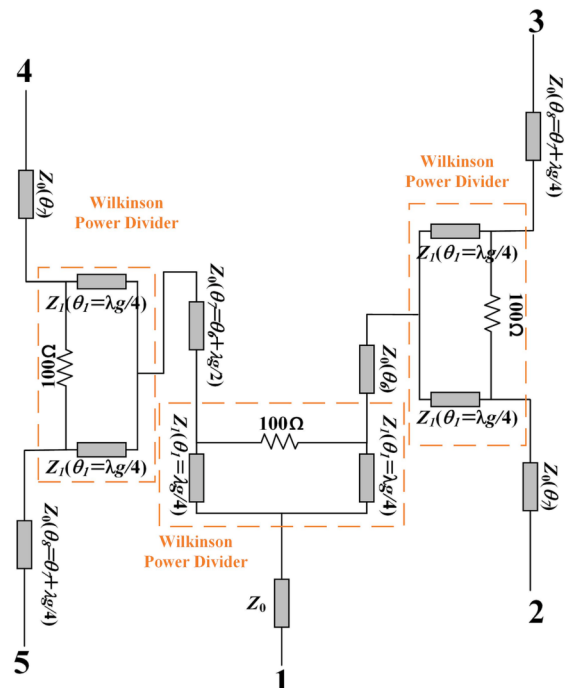
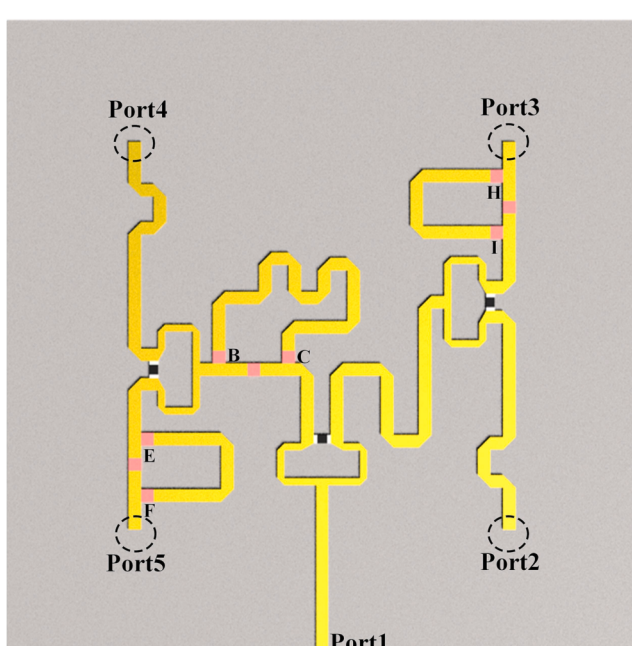


:Transmission lines where the signal cannot pass.



(a)

Fig. 5. Path of feed network and the equivalent circuits for LHCP.



(b)

Fig. 6. Path of feed network and the equivalent circuits for RHCP.

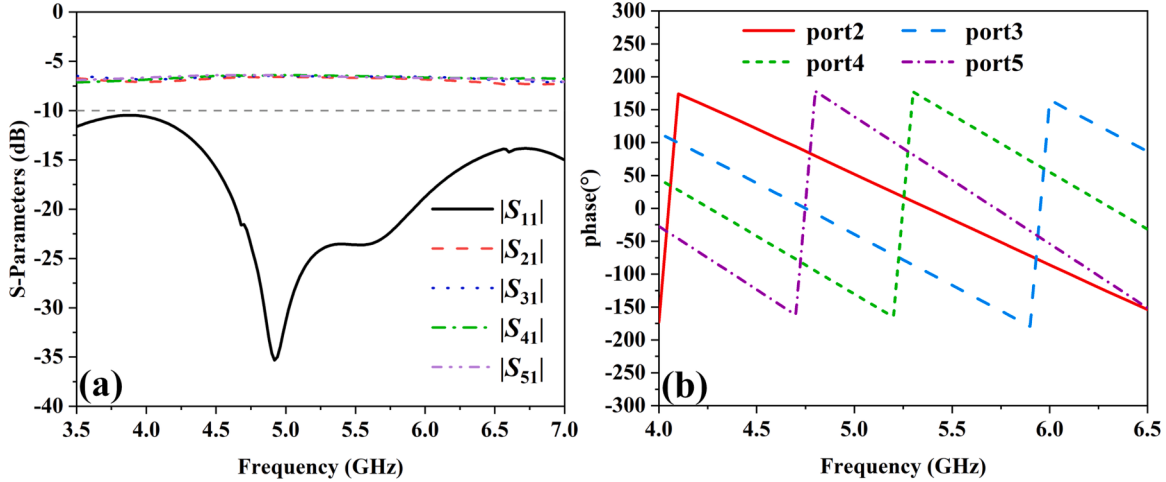


Fig. 7. Simulated results of the feeding network for LHCP: (a) Magnitude of the S-Parameters and (b) Phase difference between different ports.

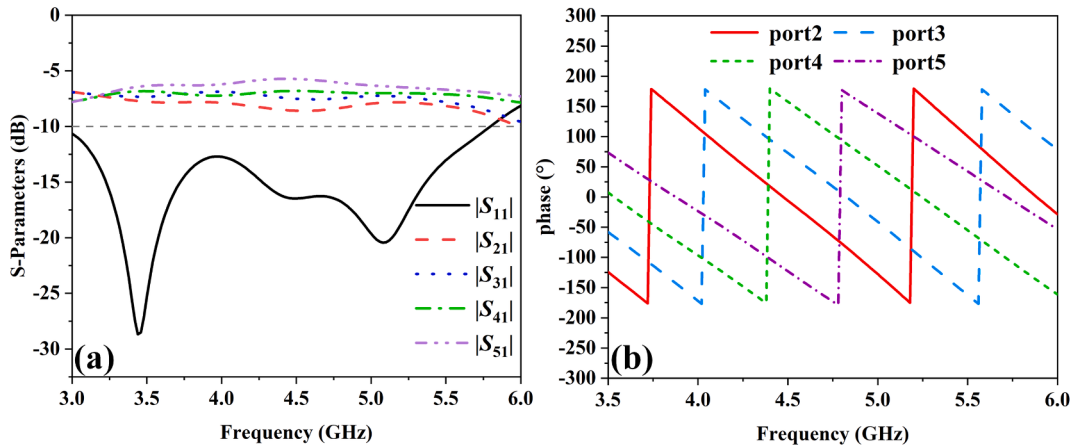


Fig. 8. Simulated results of the feeding network for RHCP: (a) Magnitude of the S-Parameters and (b) Phase difference between different ports.

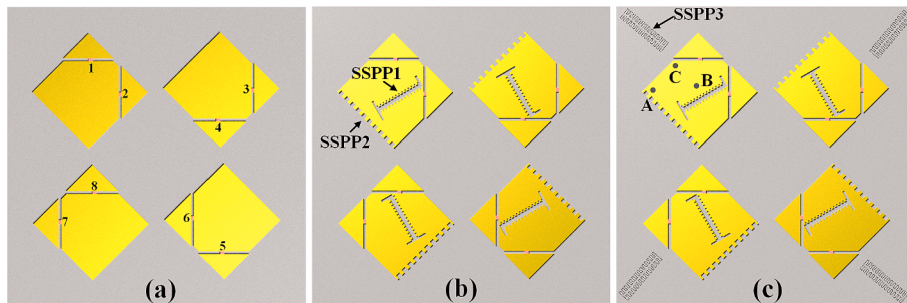


Fig. 9. (a) Step 1, (b) Step 2, and (c) Step 3 of 2x2 CP reconfigurable array design.

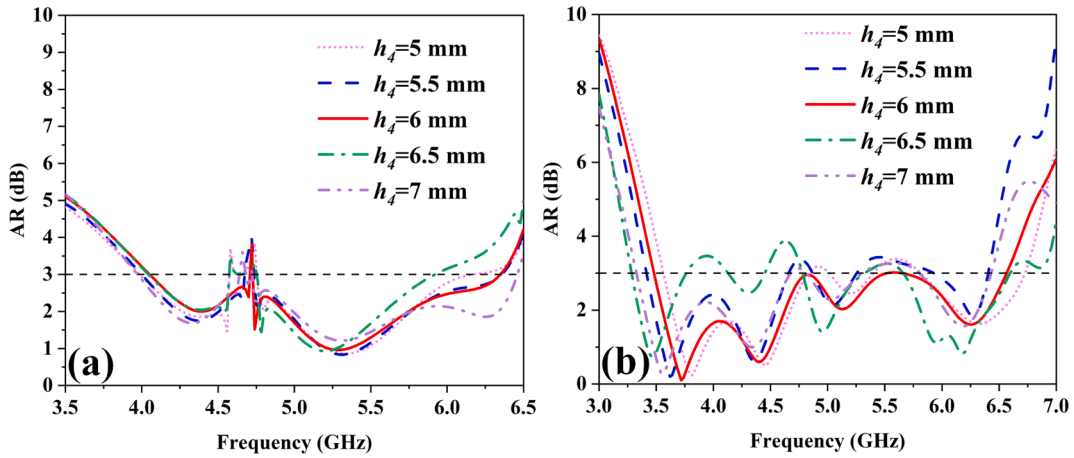
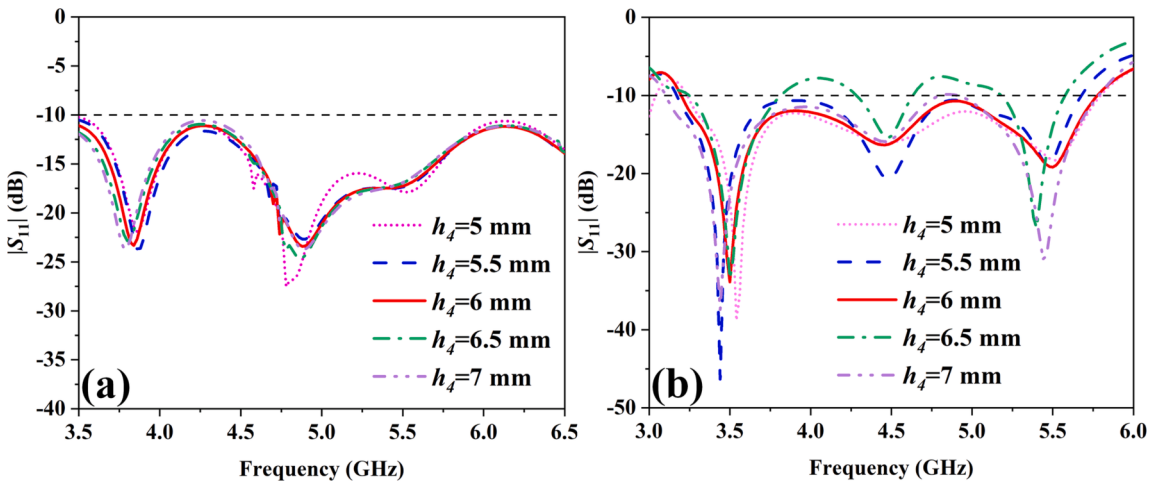
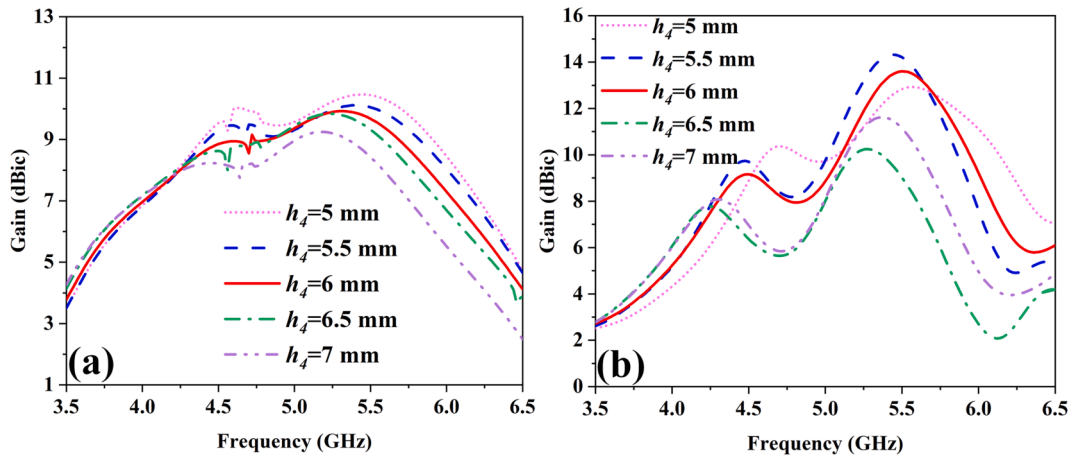
$$\epsilon(\omega) = \epsilon_\infty + \frac{\omega_p}{\omega^2 + j\omega\omega_c} \quad (6)$$

where the $e = 1.6 \times 10^{-19} C$, $m_e = 9.11 \times 10^{-31} \text{ kg}$, and $\epsilon_0 = 8.854 \times 10^{-12} \text{ F/m}$ are the electron charge, electron mass, and vacuum permittivity, respectively. From Eqs. (4) and (5), it can be seen that ω_p and ω_c are primarily determined by the free electron density n_e , neutral particle density n_n , and plasma temperature T . In this paper, ω_∞ , ω_p , and ω_c are finally determined as 12.8, $2.9 \times 10^{14} \text{ rad/s}$, and $1.65 \times 10^{13} \text{ 1/s}$, respectively [49]. The relationship between the SSP branches and the reconfigurability of the CP reconfigurable antenna could be summarized in Table 1, the corresponding circuit is in an open state when the SSPP

branch is not excited.

3.2. Reconfigurable sequential-phase feed network

Reconfigurable sequential-phase feed network adopts Wilkinson power divider to ensure the balanced distribution of input signal power. After dividing the input signal into two channels, a 90° phase difference between port2 and port3 (port4 and port5) is achieved with a $\lambda/4$ delay line, and a 180° phase difference between port3 and port4 is achieved with a $\lambda/2$ delay line. By selecting the appropriate feeds, the feed network can produce the required excitation for LHCP and RHCP, altering the transmission path of the signal.

Fig. 10. Simulated results of AR of step 1 for different h_4 : (a) LHCP, (b) RHCP.Fig. 11. Simulated results of $|S_{11}|$ of step 1 for different h_4 : (a) LHCP, (b) RHCP.Fig. 12. Simulated results of gain of step 1 for different h_4 : (a) LHCP, (b) RHCP.

Figs. 5 and 6 illustrate the feed path and equivalent circuit diagrams of the reconfigurable sequential-phase feed network at LHCP and RHCP. The reconfigurable feed network can generate the required excitation for LHCP when SSP branches A, D, and G are excited. Conversely, it can provide the necessary excitation for RHCP when SSP branches B, C, E, F, H, and I are excited.

The simulation results of the sequential-phase feed network are shown in Fig. 7 when the antenna operates at LHCP. Fig. 7(a) demonstrates that the impedance bandwidth meets the requirement from 3.5 to 7.0 GHz ($|S_{11}| < -10$ dB), and the magnitudes of the four outputs are close. Fig. 7(b) shows the phase differences between these four ports. It can be seen that these four ports (Port2, 3, 4, and 5) have around 90°

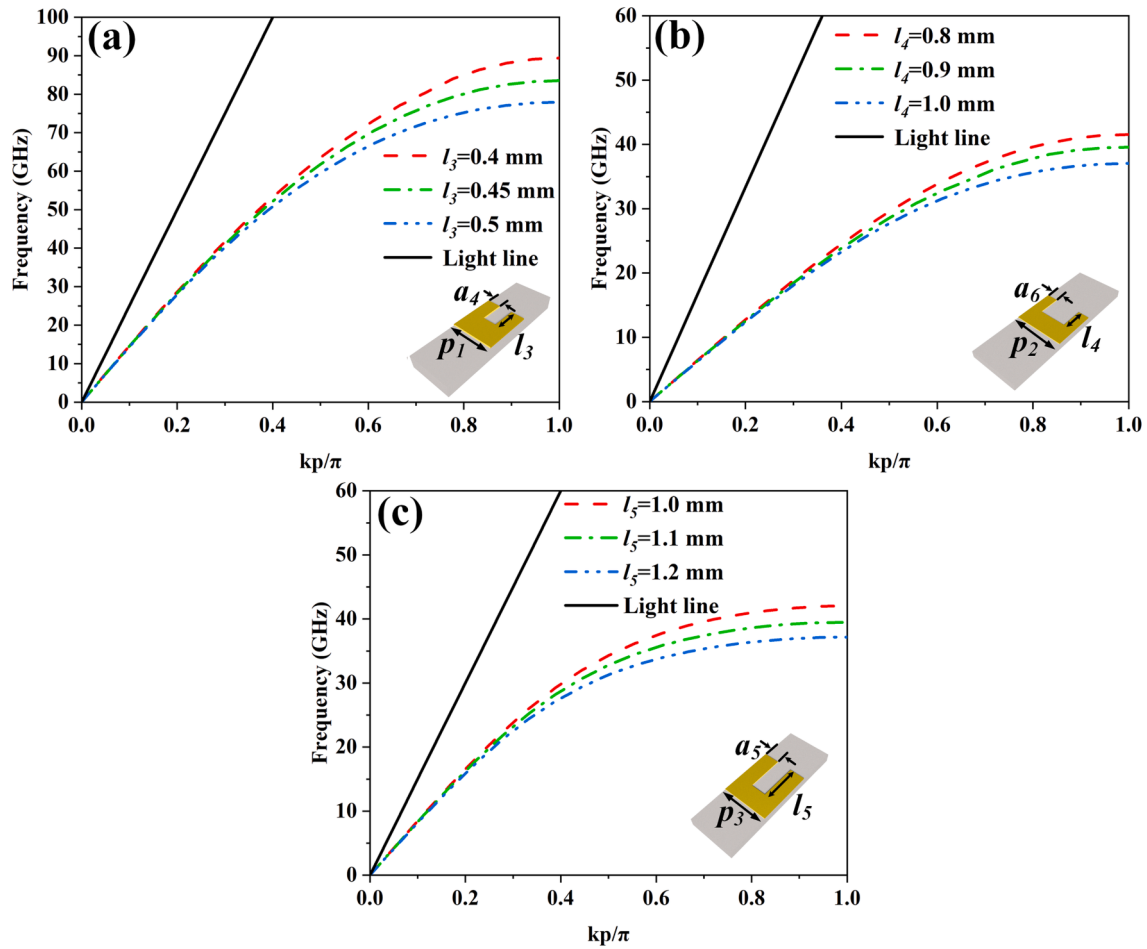


Fig. 13. Simulated dispersion diagrams of different plasmonic structures: (a) SSPP 1, (b) SSPP 2, (c) SSPP 3.

phase difference. Similarly, when the antenna operates at RHCP, Fig. 8(a) presents the impedance bandwidth of the reconfigurable feed network from 3.0 to 5.8 GHz, and the impedance bandwidth meets the requirement ($|S_{11}| < -10$ dB). The phase difference of each port (Port2, 3, 4, and 5) is almost 90° as shown in Fig. 8(b).

3.3. Gain and AR bandwidth improvement with SSPP

The reconfigurable antenna array is optimized in three steps. Step 1 is shown in Fig. 9(a), the patch adopts the form of the CP element analyzed by CMA in the previous section, without any excavation. Step 2 is formed using SSPP based on the step 1 design, as depicted in Fig. 9(b). Periodic square slots are introduced in the center and edges of the radiation patch. Moreover, SSPP structures are printed on the four corners of the lower surface of the dielectric substrate to form the step 3, as shown in Fig. 9(c).

As different SSP branches on the radiating patch are excited, the antenna can switch between LHCP and RHCP, as shown in Fig. 9(a). When the SSP branches (1, 3, 5, and 7) are excited and the others are in an open state, the antenna operates at LHCP. Conversely, when the SSP branches (2, 4, 6, and 8) are excited and the others are in an open state, the antenna operates at RHCP. In the optimization of step 1, since the height between the top and bottom substrate of the antenna has a significant effect on radiation performance, we focus on the height h_4 between the two substrate layers. It can be seen from Fig. 10(a) that the antenna operates at LHCP, AR has different degrees of deterioration at 4.5–4.8 GHz when h_3 is too high or too low, and only when $h_4 = 6$ mm, the antenna has the least AR deterioration at 4.7 GHz. Furthermore, Fig. 10(b) indicates the impact of h_4 on AR when the antenna operates at

RHCP. AR has different frequency points that do not meet the requirements from 3.75 GHz to 6.0 GHz ($AR < 3$ dB), and only when $h_4 = 6$ mm, AR is fully compliant. As shown in Fig. 11(a), it can be observed that the reflection coefficient of the antenna operating in LHCP remains essentially unchanged with the variation of h_4 . However, Fig. 11(b) reveals that when $h_4 = 6.5$ mm, there are non-compliant ($|S_{11}| < -10$ dB) regions in the reflection coefficient of the antenna at frequencies ranging from 3.83 GHz to 4.32 GHz and from 4.65 GHz to 5.23 GHz. When $h_4 = 6$ mm, the reflection coefficient in both states is less than -10 dB. Fig. 12(a) demonstrates that when $h_4 = 5$ mm, the antenna operating in LHCP achieves maximum gain. Compared to 5 mm, when $h_4 = 6$ mm, the peak gain decreases by approximately 0.66 dBic. Fig. 12(b) reveals that when the antenna is operating at RHCP, the gain of the antenna is depressed at 4.9 GHz, which indicates that further optimization of the antenna is needed. When $h_4 = 6$ mm, the peak gain of the antenna decreases by about 0.7 dBic compared with 5 mm. Consequently, considering the AR and reflection coefficient, $h_4 = 6$ mm is considered to be the best option.

The step1 antenna still has certain indicators that do not meet the standard after optimization. Specifically, as discussed above, when operating in LHCP, there are frequency points where AR has deteriorated and the gain is depressed at 4.9 GHz in RHCP. To address these shortcomings, SSPP technology is adopted. The SSPP wave is a surface EM wave that propagates along periodic metal grating structures in a slow wave form. SSPP exhibits strong confinement and advantages such as easy parameter control. As a significant method for studying its characteristics, dispersion parameters are influenced by key physical parameters, including unit width, spacing between metal gratings, and depth of the metal grating. The propagation constant β associated with the geometric parameters of the SSPP unit is expressed by Eq. (7) [48].

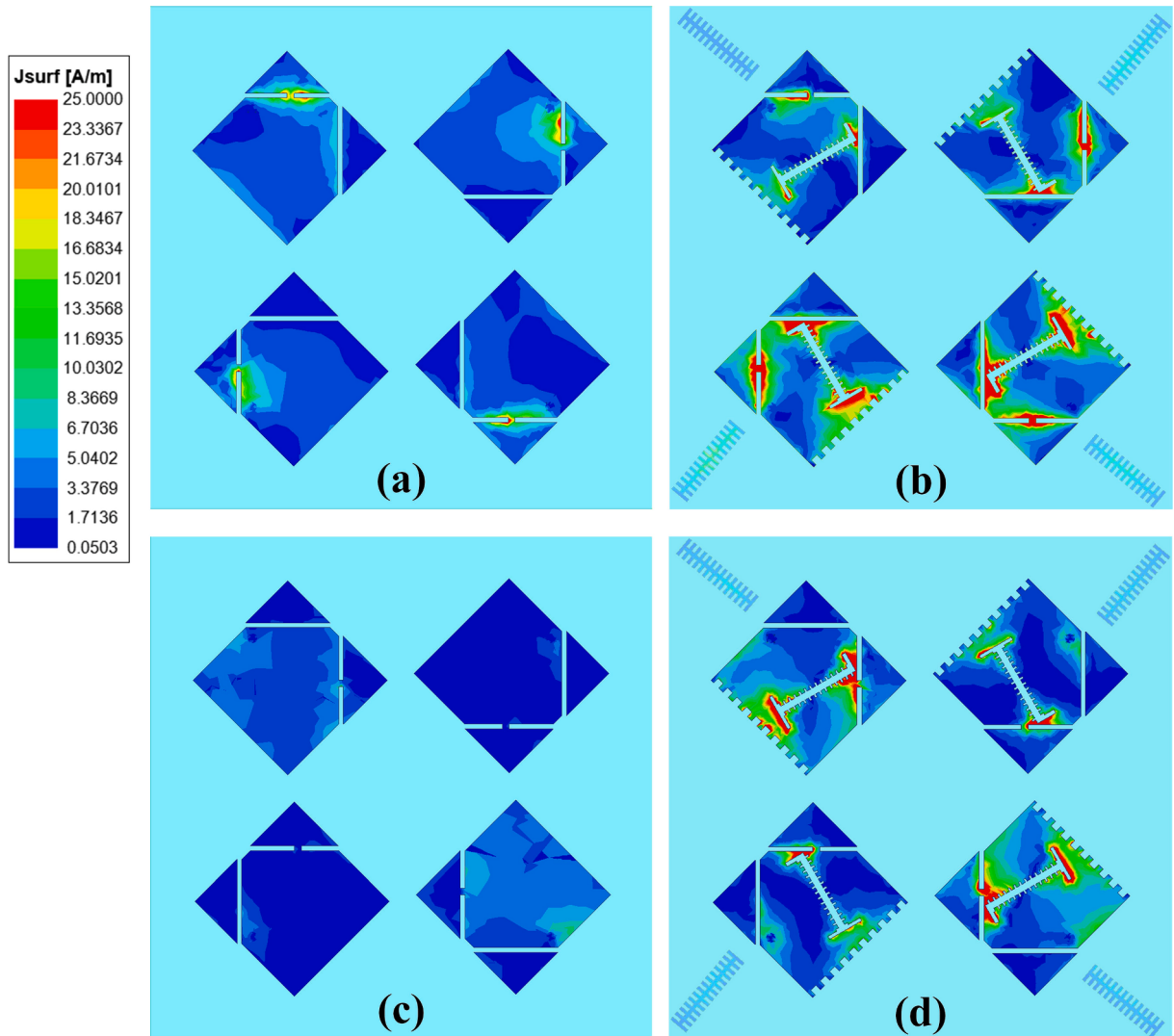


Fig. 14. Current graph of radiation patches of LHCP at 4.7 GHz: (a) Step 1, (b) Step 3 and RHCP at 4.9 GHz: (c) Step 1, (d) Step 3.

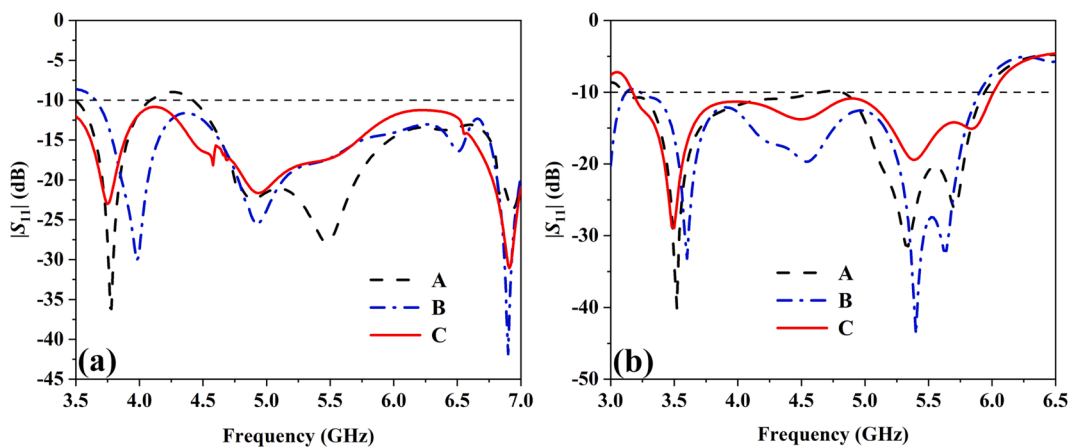


Fig. 15. Comparison of $|S_{11}|$ for different feeding points: (a) LHCP, (b) RHCP.

$$\beta = k_0 \sqrt{1 + (v/U)^2 \tan^2(k_0 h)} \quad (7)$$

where k_0 represents the free-space wave vector, v denotes the unit width, U represents the spacing between metal gratings, and h represents the

depth of the metal grating. The transverse electric field (E_t) on one side of the SSPP transmission line decays exponentially and can be expressed as Eq. (8) [19].

$$H_t(x, y) = A_n e^{-\alpha y} e^{-j\beta x} \quad (8)$$

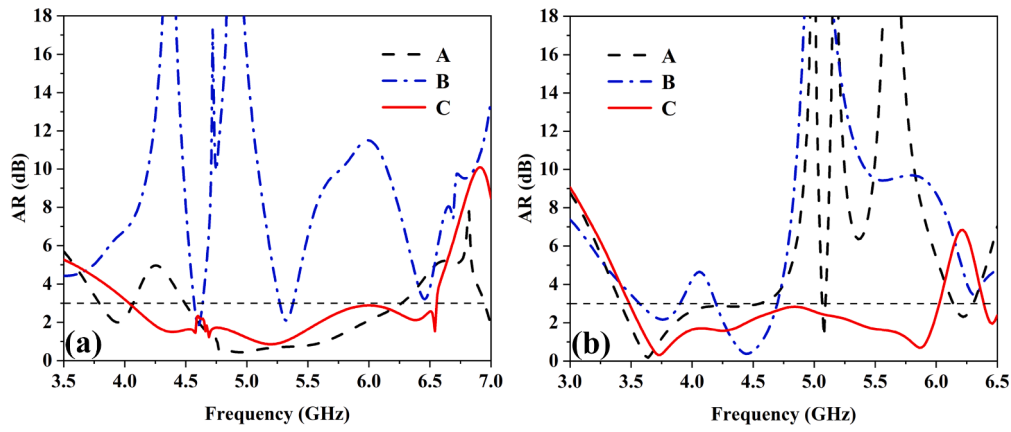


Fig. 16. Comparison of AR for different feeding points: (a) LHCp, (b) RHCp.

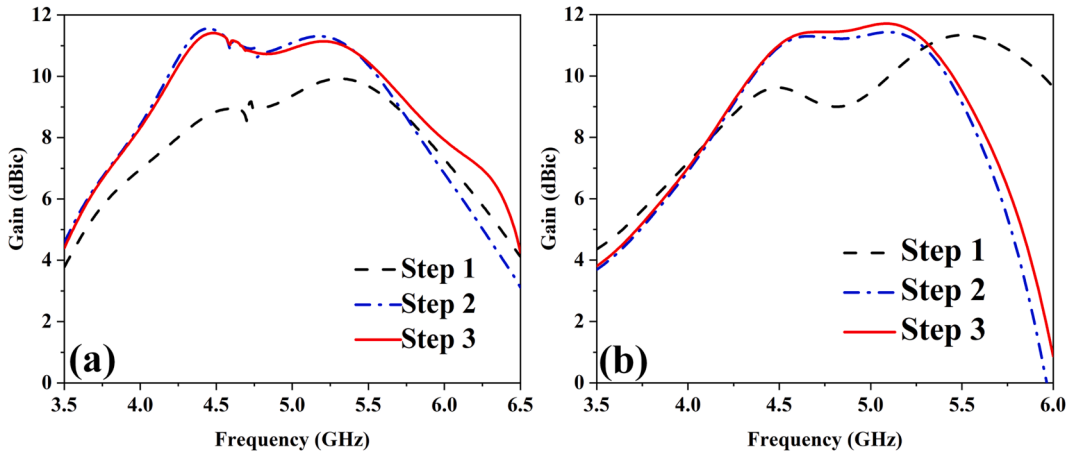


Fig. 17. Comparison of gain in three steps: (a) LHCp, (b) RHCp.

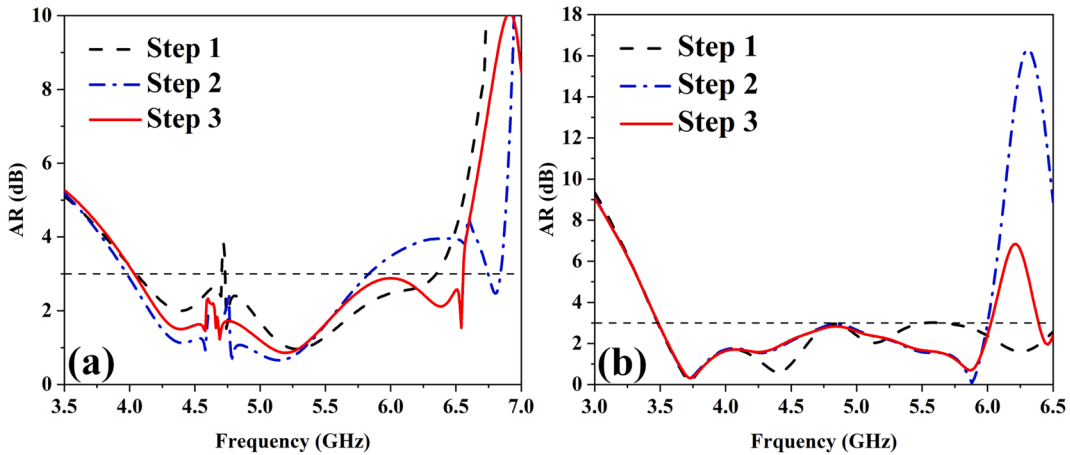


Fig. 18. Comparison of AR in three steps: (a) LHCp, (b) RHCp.

$$E_t(x, y) = \frac{-\alpha}{j\omega\epsilon_0} A_n e^{-\alpha y} e^{-j\beta x} \quad (9)$$

$$\beta^2 - \alpha^2 = k_0^2 \quad (10)$$

where A_n is a constant and ϵ_0 is the relative dielectric constant of the metal. The SSPP mode exhibits as an inhomogeneous plane wave on the propagating side, with the confinement of the plasma surface wave

dependent on the attenuation constant α . The confinement ability of the electromagnetic field decreases as α decreases, indicating a larger lateral field extension into free space. Combining Eqs. (10) and (8), Eq. (11) [48] can be obtained:

$$\alpha = \frac{k_0 v \tan(k_0 h)}{U} \quad (11)$$

Eq. (11) indicates that we can adjust the attenuation constant α and

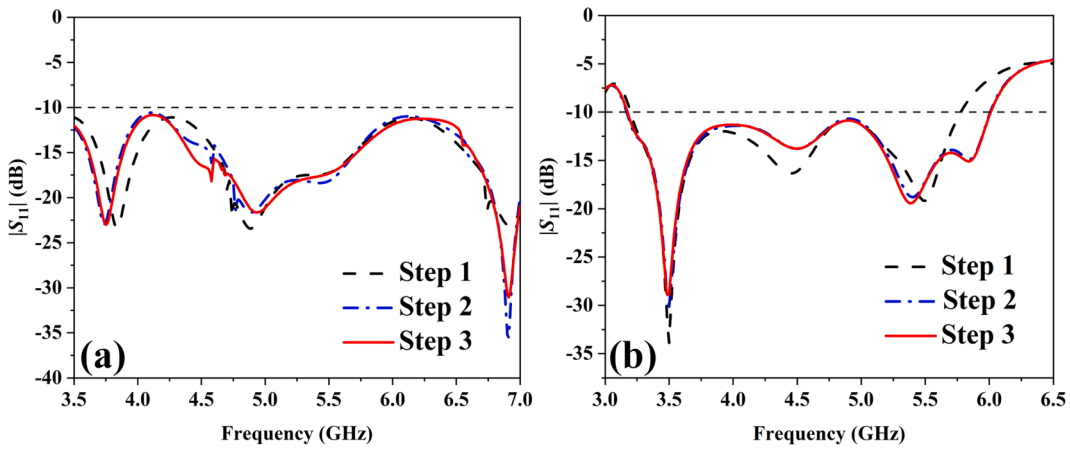
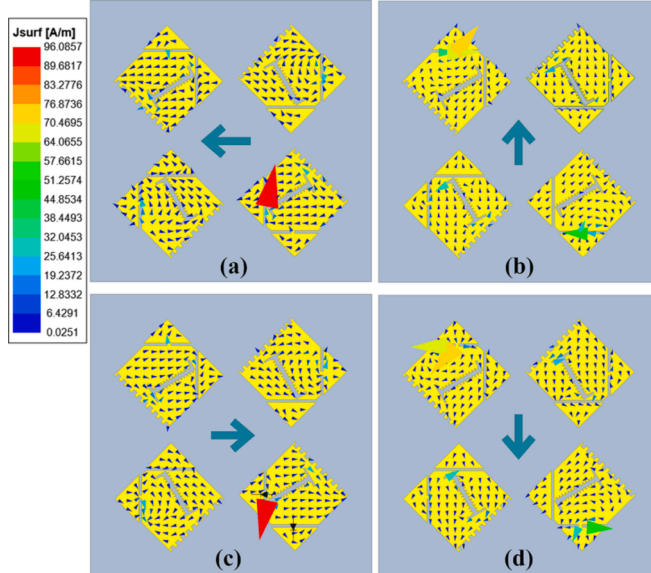
Fig. 19. Comparison of $|S_{11}|$ in three steps: (a) LHCP, (b) RHCP.

Fig. 20. Current distribution at 5 GHz of LHCP: (a) 0°, (b) 90°, (c) 180°, and (d) 270°.

control the lateral field extension by changing the value of h . Specifically, when the frequency is constant, a larger h leads to a lower cutoff frequency, as well as larger wave vectors and propagation constants, thus enhancing the confinement ability of the surface EM wave. Therefore, in the design SSPP related microwave devices, we can adjust the cutoff frequency or dispersion characteristics by controlling the depth of the metal grating.

Based on the analysis above, the depth of the metal grating is discussed as the main parameter. The dispersion curves of the different SSPP units and the light line are depicted in Fig. 13. It can be seen from Fig. 13 that the dispersion curve of the unitary structure of these three SSPPs is situated to the right of the light line, indicating slow-wave transmission and hence demonstrating that the periodic structure has a binding force on surface EM waves, ultimately leading to improving the antenna gain.

Further optimization is still needed for AR and gain in Step 1. Therefore, a comparison of current distribution between Step 3 with SSPP loading and Step 1 is performed, as shown in Fig. 14. During the design process of Step 1, when the antenna operates at LHCP, there are still non-compliant regions in AR at 4.7 GHz. Therefore, the current distribution between Step 3 and Step 1 at 4.7 GHz is compared for LHCP

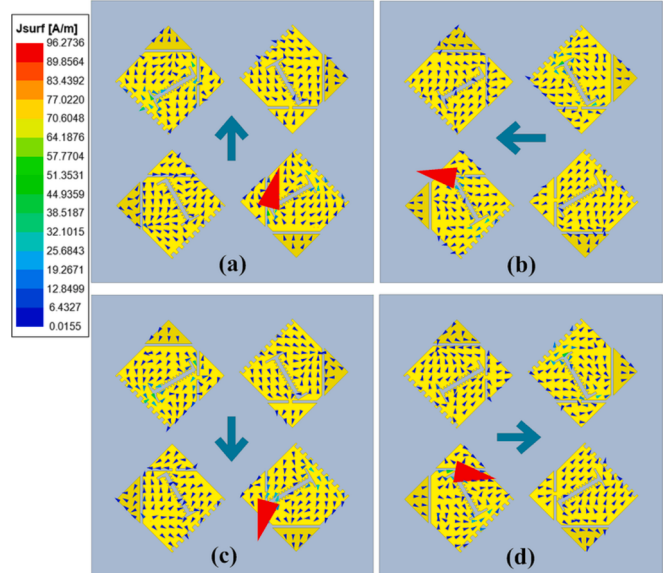


Fig. 21. Current distribution at 5 GHz of RHCP: (a) 0°, (b) 90°, (c) 180°, and (d) 270°.

operation, as shown in Fig. 14(a) and (b). When the antenna operates at RHCP, a significant dip is observed at 4.9 GHz in the antenna of Step 1. Thus, the current distribution between Step 3 and Step 1 at 4.9 GHz is compared for RHCP operation, as shown in Fig. 14(c) and (d). By comparison, it is found that the energy on the patch loaded with SSPP has become more concentrated around the metal grid, and as mentioned before, SSPP has played a certain binding effect on EM waves.

The excitation structure of characteristic modes can be divided into inductive coupling excitation (ICE) and capacitive coupling excitation (CCE) structures. For electric field-coupled excitation, CCE structures can be placed at the minimum characteristic current or maximum electric field locations. On the other hand, for magnetic field-coupled excitation, ICE structures can be placed at the locations of maximum characteristic current or magnetic field. Furthermore, the research results demonstrate that the impact of ICE excitation structures on the characteristic modes of the original structure is relatively small compared to CCE excitation structures [50]. In the discussed antenna, a CCE feeding structure is utilized. The characteristic currents shown in Fig. 3 indicate that the feeding point should be placed at either point A or B in Fig. 9(c). However, following the adoption of the SSPP structure, the energy of the radiating patch becomes more focused around the metal grid,

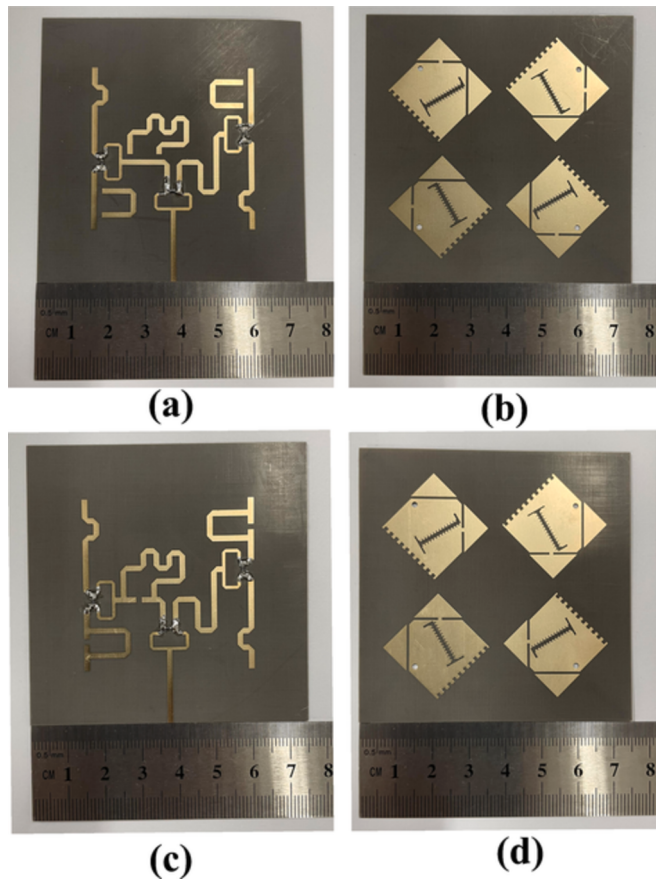


Fig. 22. Photograph of the fabricated equivalent prototype: (a) Feed network of LHCP, (b) Radiation patch of LHCP, (c) Feed network of RHCP, (d) Radiation patch of RHCP.

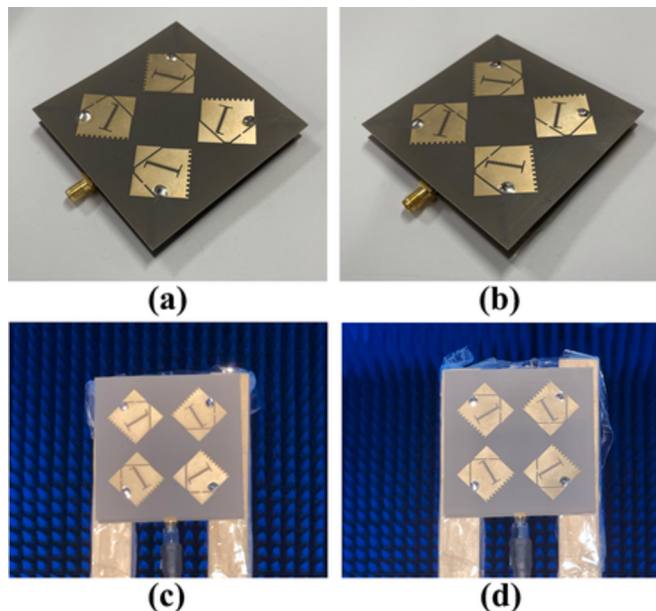


Fig. 23. The equivalent assembled prototype array and microwave anechoic chamber measurement diagram: (a) Assembled array of LHCP, (b) Assembled array of RHCP, (c) Measurement of LHCP, (d) Measurement of RHCP.

influencing the initial characteristic currents. As a result, point C is identified as a new feeding point, as demonstrated in Fig. 9(c).

The reflection coefficient of different feeding points is depicted in Fig. 15. It can be observed that when located at point A, the impedance matching experiences slight degradation. Fig. 16 presents the AR of the three feeding points. When an external current source is applied at points A and B, the AR of two CP states undergoes significant degradation, which is consistent with the previous discussion that energy becomes localized at the metal grid after the SSPP structure is implemented. Therefore, point C is reselected as the new CCE excitation point, at which both impedance matching and AR exhibit good performance.

Fig. 17 depicts a comparison of the gain for three steps, demonstrating that the overall antenna gain for both polarizations is substantially improved from 4.3 to 5.2 GHz with the loading of the SSPP. Fig. 17(a) shows that when the antenna operates at LHCP, the gain of the antenna at 4.4 GHz is increased from 8.6 to 11.3 dBic. Fig. 17(b) shows that when the antenna operates at RHCP, the gain of the antenna at 4.8 GHz is increased from 9 to 11.5 dBic. This further demonstrates that the confinement of EM waves by SSPP plays a significant role in enhancing the antenna gain. Fig. 18 depicts a comparison of the AR for three steps. As seen in Fig. 18(a), when the antenna operates at LHCP, the AR of Step 2 at 4.6 GHz still does not meet the requirement compared to Step 1, while Step 3 shows a significant optimization over Steps 1 and 2, and the AR of step3 exhibits a broader bandwidth of 0.9 GHz compared to step2. This is due to the suppression effect of the SSPP structure loaded at the bottom of the dielectric substrate on the surface waves. Fig. 18(b) shows that when the antenna operates at RHCP, the AR of Step 3 and Step 2 has no significant change, but compared with Step 1, the effective band of AR is moved from 6.5 GHz to 6 GHz after loading SSPP, although there is a part of shrinkage, the gain of the antenna at the center frequency point has a significant improvement, so it is considered worthwhile. Fig. 19 depicts a comparison of the reflection coefficient for three steps. It can be seen from Fig. 19(a) and (b) that loading SSPP has no significant effect on the reflection coefficient of the antenna, regardless of whether the antenna is operating at LHCP or RHCP.

In light of the close relationship between the phase rotation of an antenna and its electric field vector, Figs. 20 and 21 depict the current distribution of the antenna in LHCP and RHCP at 0°, 90°, 180°, and 270° at 5 GHz. Due to the excitation of the sequential phase feed network, it is evident that the radiation patch exhibits current distributions at 0°, 90°, 180°, and 270° that are mutually orthogonal. The current in Fig. 20 exhibits clockwise rotation, thus confirming that the antenna operates at LHCP. Conversely, Fig. 21 highlights the counterclockwise rotation of the current, thereby indicating that the antenna operates at RHCP.

4. Experimental verification

To verify this CP reconfigurable antenna array design, the final optimized model is fabricated and tested. Due to limitations in fabrication conditions, it is difficult to directly fabricate the antenna by loading a real SSP. Therefore, it is necessary to use copper as a substitute for SSP to fabricate an equivalent model, as shown in Fig. 22. Fig. 23(a) and (b) depict the equivalent feed network and radiation patch of the antenna operating at LHCP, respectively. Fig. 22(c) and (d) show the equivalent feed network and radiation patch of the antenna operating at RHCP, respectively. The antenna array is successfully assembled and positioned within an antenna chamber for the test, as shown in Fig. 23.

Fig. 24 shows the measured $|S_{11}|$ of the fabricated antenna at two CP states. As demonstrated in Fig. 24(a) and (b), the measured relative impedance bandwidth is 114.7% (2.08 to 7.68 GHz) in the LHCP state and 72.8% (2.88 to 6.16 GHz) in the RHCP state. The simulation results fit the measured results well. Moreover, the measured AR curves are shown in Fig. 25. Fig. 25(a) shows that when the antenna operates at LHCP, the measured AR bandwidth is 38.5% (4.15 to 6.13 GHz), which is a reduction of 0.5 GHz compared to the simulated result of 47.4%

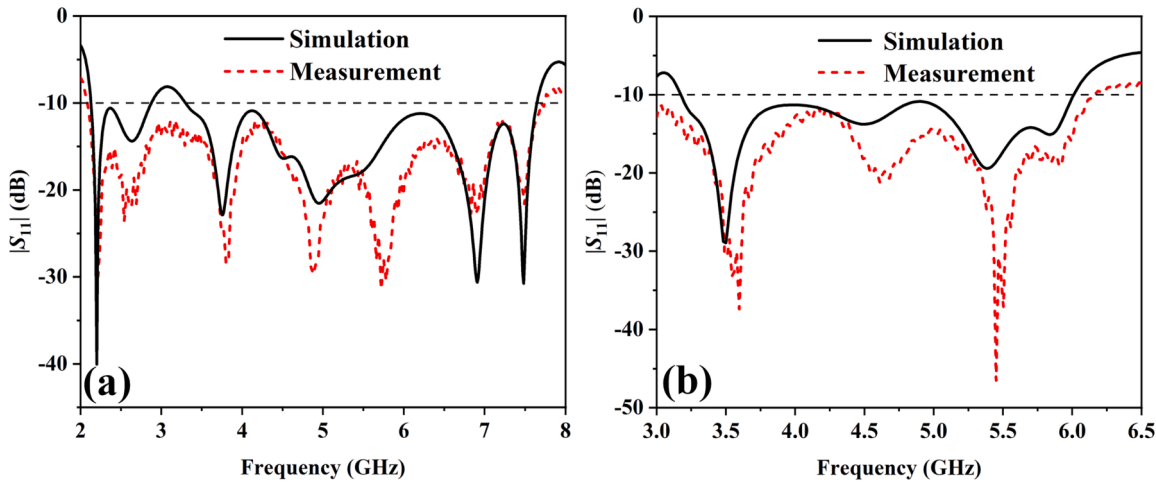
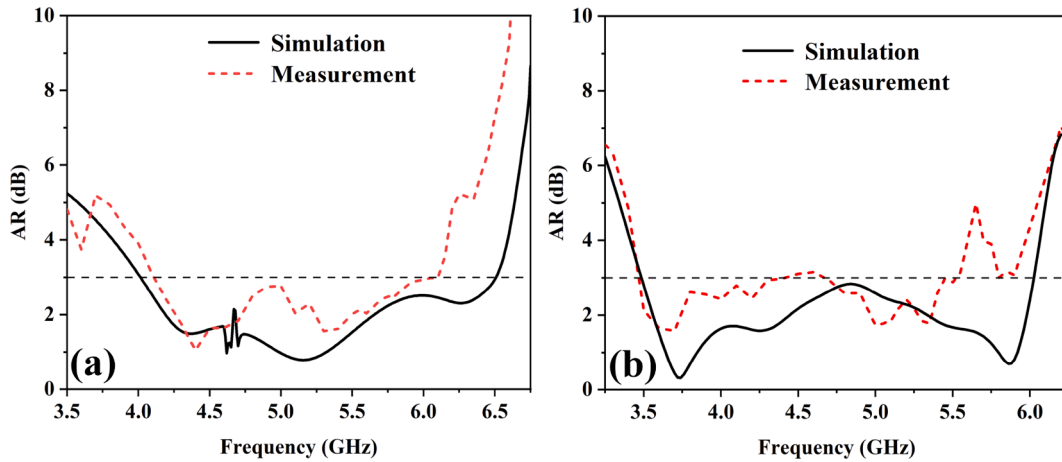
Fig. 24. Comparison of simulated and measured $|S_{11}|$: (a) LHCP, (b) RHCP.

Fig. 25. Comparison of simulated and measured AR: (a) LHCP, (b) RHCP.

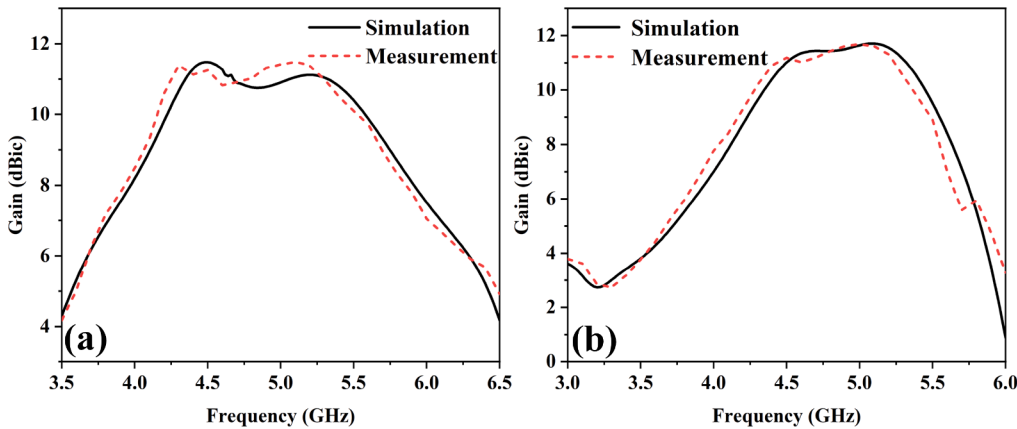


Fig. 26. Comparison of simulated and measured gain: (a) LHCP, (b) RHCP.

(4.01 to 6.5 GHz) at high frequencies. Additionally, Fig. 25(b) demonstrates that when the antenna operates at RHCP, the measured AR bandwidth is 42.6 % (3.45 to 4.48 GHz, 4.68 to 5.57 GHz), which is a slight degradation of 0.2 GHz in the central frequency point compared to the simulated result of 53.1 % (3.5 to 6.03 GHz). This could be due to the slight deformation of the dielectric substrate caused by the heating during the antenna soldering process or potential errors during the

measurement. The measurement results of antenna gain are shown in Fig. 26. Fig. 26(a) demonstrates that when the antenna operates at LHCP, the measured gain is consistent with the simulation, with an improvement of approximately 0.4 dBic in the range of 5 GHz to 5.25 GHz, and a peak gain of 11.48 dBic. Fig. 26(b) shows that when the antenna operates at RHCP, the gain experiences a shift of approximately 0.1 GHz towards lower frequencies in the center frequency range, with a

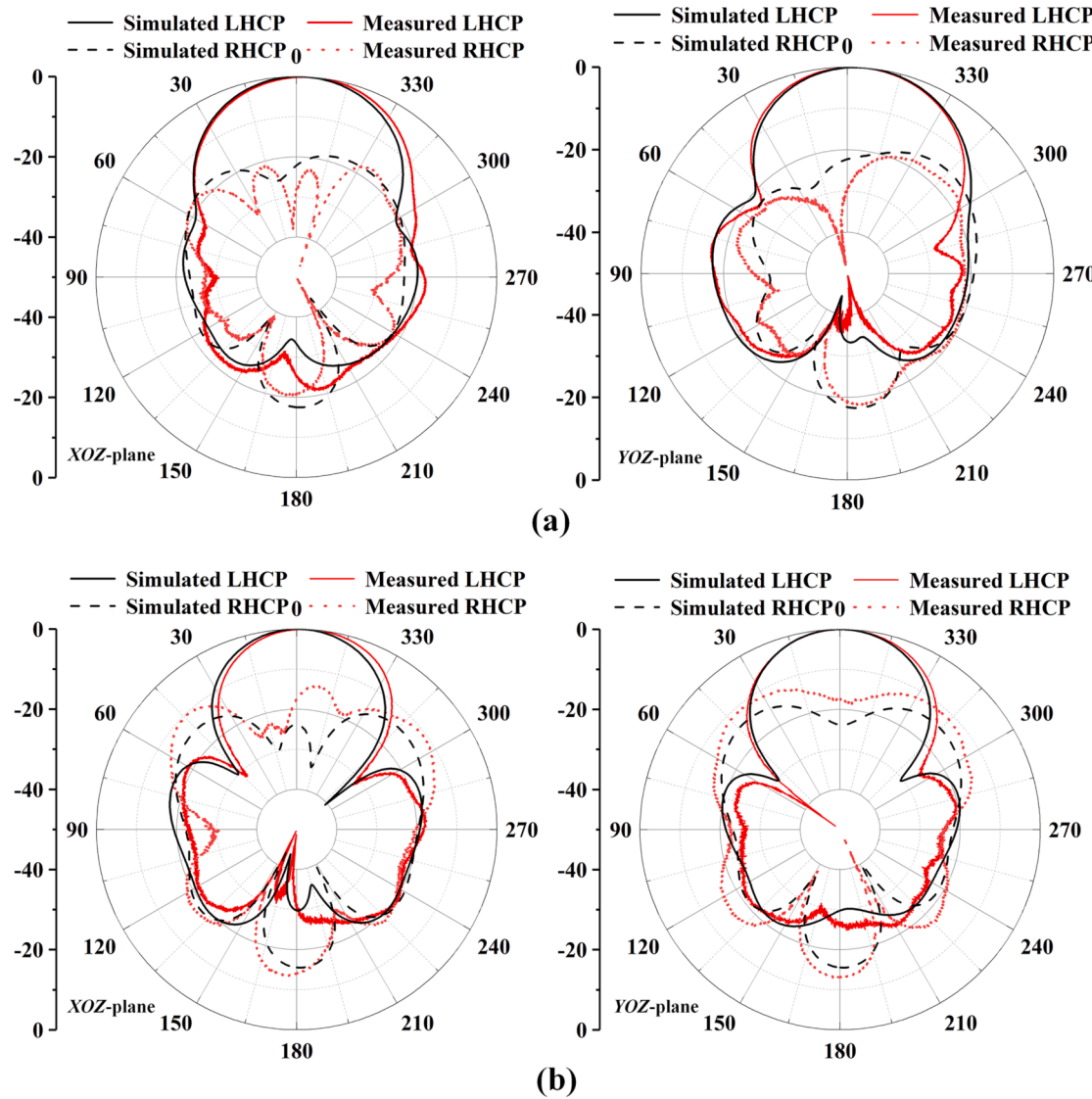


Fig. 27. The simulated and measured normalized patterns at LHCP state: (a) 4.4 GHz, (b) 5 GHz.

peak gain of 11.68 dBic. These errors are likely caused by the fabrication process.

The far-field radiation patterns of the two planes simulated and measured are plotted in Fig. 27 and Fig. 28, respectively. Fig. 27(a) and (b) respectively illustrate the radiation patterns at 4.4 GHz and 5 GHz when the antenna operates at LHCP. The isolation of the RHCP and LHCP in the broadside direction ($\theta = 0^\circ$) at 4.4 GHz can reach 28.1 dB and 28.4 dB at the xoz and yoz planes, respectively, (17.2 dB and 17.8 dB for two planes at 5 GHz). Fig. 28(a) and (b) respectively depict the radiation patterns at 3.9 GHz and 4.8 GHz when the antenna operates at RHCP. At this state, the isolation at 3.9 GHz can reach 16.9 dB and 18.5 dB at the xoz and yoz planes, (18.8 dB and 17.7 dB for two planes at 4.8 GHz). The measured results show that the radiation patterns of the proposed array has good symmetry and stable orientation, and the measurement agrees well with the simulation.

Table 2 presents a comparison of the performance of the proposed CP reconfigurable antenna with other polarization-reconfigurable antennas in recent years. The antenna has a smaller size and a larger overlapped bandwidth in comparison. Although the gain of Refs. [3] and [13] is higher, meanwhile the lateral dimensions of the antenna are much larger. Compared with Refs. [8] and [12], the proposed antenna exhibits a smaller size, higher gain, and wider bandwidth. In summary, we have demonstrated a compact, wide bandwidth, and high-gain CP

reconfigurable antenna array.

5. Conclusion

A high-gain and wideband CP reconfigurable antenna array with a size of only $1.0\lambda \times 1.0\lambda \times 0.09\lambda$ based on SSP has been presented in this paper. The antenna can achieve the switching between LHCP and RHCP by manipulating different SSP branches on the feeding network and radiation patch. The measurement results indicate that when the antenna operates at LHCP, it exhibits an impedance bandwidth of 114.7 % (2.08 to 7.68 GHz), an AR bandwidth of 38.5 % (4.15 to 6.13 GHz), and a peak gain of 11.48 dBic. When the antenna operates at RHCP, it has an impedance bandwidth of 72.8 % (2.88 to 6.16 GHz), an AR bandwidth of 42.6 % (3.45 to 4.48 GHz, 4.68 to 5.57 GHz), and a peak gain of 11.68 dBic. The proposed antenna has potential applications in wideband and multi-polarization wireless platforms, increasing overall channel capacity and mitigating polarization mismatch issues in complex channels.

Declaration of Competing Interest

The authors declare that they have no known competing financial interests or personal relationships that could have appeared to influence the work reported in this paper.

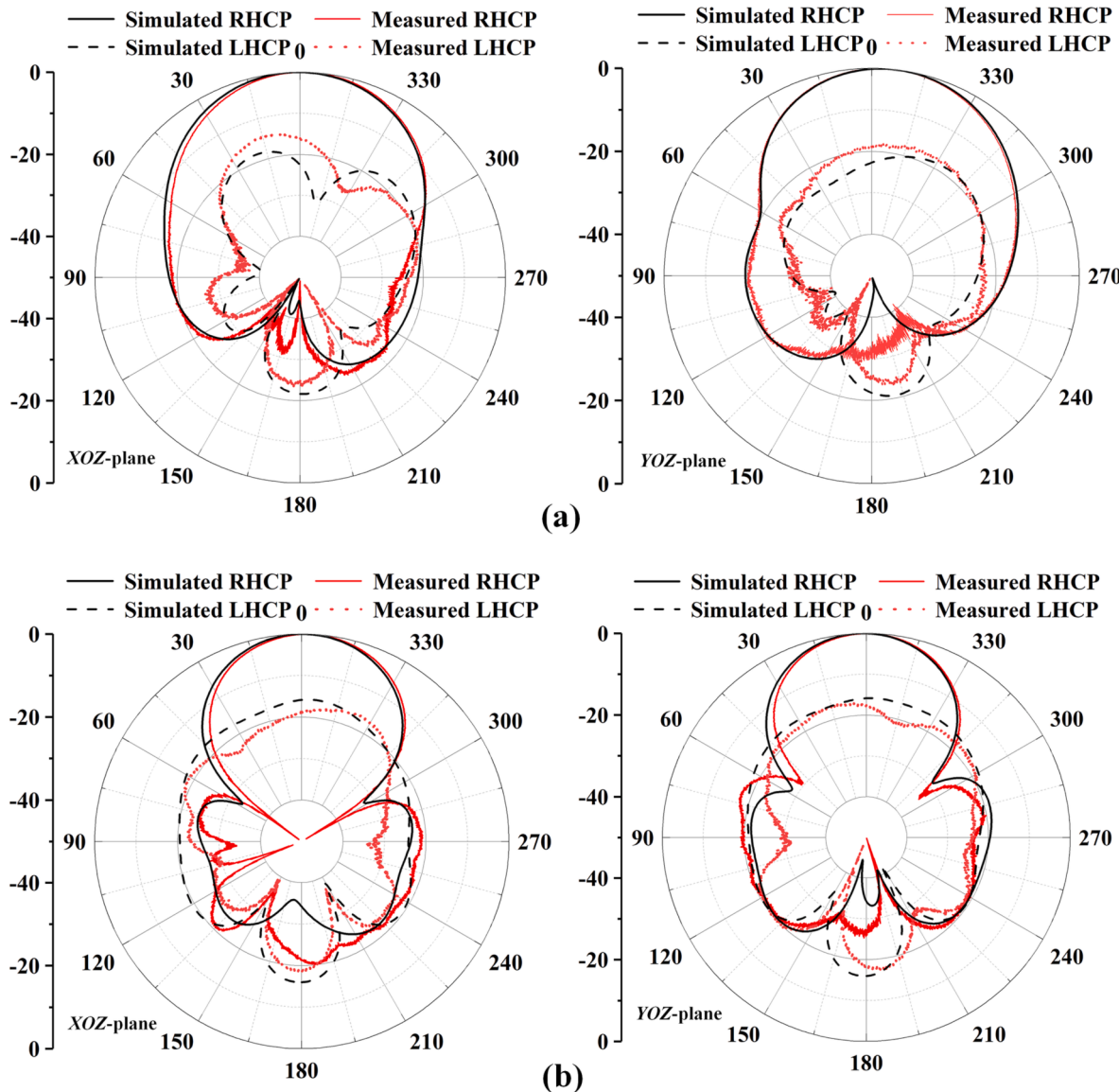


Fig. 28. The simulated and measured normalized patterns at RHCP state: (a) 3.9 GHz, (b) 4.8 GHz.

Table 2
Comparison with other antennas.

Ref.	Size (λ^3)	$ S_{11} $ BW (%)		AR BW(%)		Peak gain (dBi)	
		LHCP	RHCP	LHCP	RHCP	LHCP	RHCP
[3]	$2.41 \times 2.41 \times 0.062$	41.2	41.2	31.6	31.6	16.3	16.3
[5]	$0.56 \times 0.56 \times 0.037$	7.1	7.5	6.25	7.1	6.63	6.5
[8]	$2.64 \times 2.83 \times 0.062$	27.2	27.2	17.5	19	9.9	9.85
[12]	$1.83 \times 1.83 \times 0.6$	25.0	25.0	13.5	13.5	11.2	11.2
[13]	$1.65 \times 2.05 \times 0.25$	18	18	14.5	15.0	14.0	14.2
Proposed	$1.0 \times 1.0 \times 0.09$	114.7	72.8	38.5	42.6	11.48	11.68

References

- [1] S. Wang, D. Yang, W. Geyi, C. Zhao, G. Ding, Polarization-Reconfigurable Antenna Using Combination of Circular Polarized Modes, *IEEE Access* 9 (2021) 45622–45631.
- [2] D. Piazza, P. Mookiah, M. D'Amico, K.R. Dandekar, Experimental Analysis of Pattern and Polarization Reconfigurable Circular Patch Antennas for MIMO Systems, *IEEE Trans. Veh. Technol.* 59 (5) (2010) 2352–2362.
- [3] Q.-C. Ye, J.-L. Li, Y.-M. Zhang, A Circular Polarization-Reconfigurable Antenna With Enhanced Axial Ratio Bandwidth, *IEEE Antennas Wireless Propag. Lett.* 21 (6) (2022) 1248–1252.
- [4] C.-Y.-D. Sim, Y.-J. Liao, H.-L. Lin, Polarization Reconfigurable Eccentric Annular Ring Slot Antenna Design, *IEEE Trans. Antennas Propag.* 63 (9) (2015) 4152–4155.
- [5] M. Li, Z. Zhang, M.-C. Tang, A Compact, Low-Profile, Wideband, Electrically Controlled, Tri-Polarization-Reconfigurable Antenna With Quadruple Gap-Coupled Patches, *IEEE Trans. Antennas Propag.* 68 (8) (2020) 6395–6400.
- [6] J.-S. Row, C.-J. Shih, Polarization-Diversity Ring Slot Antenna With Frequency Agility, *IEEE Trans. Antennas Propag.* 60 (8) (2012) 3953–3957.
- [7] L. Ge, X. Yang, D. Zhang, M. Li, H. Wong, Polarization-Reconfigurable Magnetoelectric Dipole Antenna for 5G Wi-Fi, *IEEE Antennas Wireless Propag. Lett.* 16 (2017) 1504–1507.
- [8] J. Hu, Z.-C. Hao, W. Hong, Design of a Wideband Quad-Polarization Reconfigurable Patch Antenna Array Using a Stacked Structure, *IEEE Trans. Antennas Propaga.* 65 (6) (2017) 3014–3023.
- [9] B. Liu, J. Qiu, C. Wang, N. Wang, G. Li, Rectangular dielectric resonator antenna with polarization reconfigurable characteristic, *Microw. Opt. Technol. Lett.* 61 (3) (2019) 766–771.

- [10] X. Ding, Z. Zhao, Y. Yang, Z. Nie, Q.H. Liu, Wideband Quad-Polarization Reconfigurable Antenna Using Switchable Feed Network With Stable Unidirectional Radiation Patterns, *IEEE Access* 6 (2018) 73434–73443.
- [11] W. Lin, H. Wong, Wideband Circular-Polarization Reconfigurable Antenna With L-Shaped Feeding Probes, *IEEE Antennas Wireless Propag. Lett.* 16 (2017) 2114–2117.
- [12] L.-Y. Ji, P.-Y. Qin, Y.J. Guo, C. Ding, G. Fu, S.-X. Gong, A Wideband Polarization Reconfigurable Antenna With Partially Reflective Surface, *IEEE Trans. Antennas Propag.* 64 (10) (2016) 4534–4538.
- [13] N. Zhu, X.-X. Yang, T. Lou, Q. Cao, S. Gao, Broadband Polarization-Reconfigurable Slot Antenna and Array With Compact Feed Network, *IEEE Antennas Wireless Propag. Lett.* 18 (6) (2019) 1293–1297.
- [14] W. Lin, S.-L. Chen, R.W. Ziolkowski, Y.J. Guo, Reconfigurable, Wideband, Low-Profile, Circularly Polarized Antenna and Array Enabled by an Artificial Magnetic Conductor Ground, *IEEE Trans. Antennas Propag.* 66 (3) (2018) 1564–1569.
- [15] H.H. Tran, C.D. Bui, N. Nguyen-Trong, T.K. Nguyen, A Wideband Non-Uniform Metasurface-Based Circularly Polarized Reconfigurable Antenna, *IEEE Access* 9 (2021) 42325–42332.
- [16] A.P. Hibbins, B.R. Evans, J.R. Sambles, Experimental Verification of Designer Surface Plasmons, *Sci. New Ser.* 308 (5722) (2005) 670–672.
- [17] P. Nagpal, N.C. Lindquist, S.-H. Oh, D.J. Norris, Ultrasmooth Patterned Metals for Plasmonics and Metamaterials, *Science* 325 (5940) (2009) 594–597.
- [18] L. Liu, M. Chen, X. Yin, Single-Layer High Gain Endfire Antenna Based on Spoof Surface Plasmon Polaritons, *IEEE Access* 8 (2020) 64139–64144.
- [19] X.-F. Zhang, J. Fan, J.-X. Chen, High Gain and High-Efficiency Millimeter-Wave Antenna Based on Spoof Surface Plasmon Polaritons, *IEEE Trans. Antennas Propag.* 67 (1) (2019) 687–691.
- [20] H. Zhao, J. Li, Q. Zhang, S. Li, X. Yin, Spoof Surface Plasmon Polariton Antenna With Dual-Band Endfire Gain and Flexible Small Frequency Ratio, *IEEE Trans. Antennas Propag.* 70 (11) (2022) 11079–11084.
- [21] L. Yang, F. Xu, T. Jiang, J. Qiang, S. Liu, J. Zhan, A Wideband High-Gain Endfire Antenna Based on Spoof Surface Plasmon Polaritons, *IEEE Antennas Wireless Lett.* 19 (12) (2020) 2522–2525.
- [22] P. Jiang, W. Jiang, S. Gong, A Mesh-Type Low RCS Reflectarray Antenna Based on Spoof Surface Plasmon Polariton, *IEEE Antennas Wireless Propag. Lett.* 20 (2) (2021) 224–228.
- [23] L. Liu, Y. Jiang, Y. Hu, D. Jiang, L. Zhu, Wideband Millimeter-Wave Endfire Antenna Based on Symmetrical Spoof Surface Plasmon Polaritons, *IEEE Trans. Antennas Propag.* 69 (11) (2021) 7386–7393.
- [24] Z.N. Chen Nasimuddin, K.P. Esselle, Wideband circularly polarized microstrip antenna array using a new single feed network, *Microw. Opt. Technol. Lett.* 50 (7) (2008) 1784–1789.
- [25] D.J. Bisharat, S. Liao, Q. Xue, Wideband Unidirectional Circularly Polarized Antenna With L-Shaped Radiator Structure, *IEEE Antennas Wireless Lett.* 16 (2017) 12–15.
- [26] Q. Liu, Z.N. Chen, Y. Liu, C. Li, Compact Ultra-Wideband Circularly-Polarized Weakly Coupled Patch Array Antenna, *IEEE Trans. Antennas Propag.* 65 (4) (2017) 2129–2134.
- [27] W. Tan, X. Shan, Z. Shen, Ultrawideband Circularly Polarized Antenna With Shared Semicircular Patches, *IEEE Trans. Antennas Propag.* 69 (6) (2021) 3555–3559.
- [28] J.-W. Baik, T.-H. Lee, S. Pyo, S.-M. Han, J. Jeong, Y.-S. Kim, Broadband Circularly Polarized Crossed Dipole With Parasitic Loop Resonators and Its Arrays, *IEEE Trans. Antennas Propaga.* 59 (1) (2011) 80–88.
- [29] R. Xu, et al., Analysis and Design of Ultrawideband Circularly Polarized Antenna and Array, *IEEE Trans. Antennas Propag.* 68 (12) (2020) 7842–7853.
- [30] R. Xu, Z. Shen, S.S. Gao, Compact-Size Ultra-Wideband Circularly Polarized Antenna With Stable Gain and Radiation Pattern, *IEEE Trans. Antennas Propag.* 70 (2) (2022) 943–952.
- [31] W. Li, Y. Zhao, X. Ding, L. Wu, Z. Nie, A Wideband Pattern-Reconfigurable Loop Antenna Designed by Using Characteristic Mode Analysis, *IEEE Antennas Wireless Propag. Lett.* 21 (2) (2022) 396–400.
- [32] A. Sharma, et al., Design of Compact Wideband Circularly Polarized Hexagon-Shaped Antenna Using Characteristics Mode Analysis, *IEEE Trans. Instrum. Meas.* 70 (2021) 1–8.
- [33] G. Gao, R.-F. Zhang, W.-F. Geng, H.-J. Meng, B. Hu, Characteristic Mode Analysis of a Nonuniform Metasurface Antenna for Wearable Applications, *IEEE Antennas Wireless Propag. Lett.* 19 (8) (2020) 1355–1359.
- [34] N.-W. Liu, L. Zhu, Z.-X. Liu, G. Fu, Y. Liu, Radiation Pattern Reshaping of a Narrow Slot Antenna for Bandwidth Enhancement and Stable Pattern Using Characteristic Modes Analysis, *IEEE Trans. Antennas Propag.* 70 (1) (2022) 726–731.
- [35] J. Zeng, X. Liang, L. He, F. Guan, F.H. Lin, J. Zi, Single-Fed Triple-Mode Wideband Circularly Polarized Microstrip Antennas Using Characteristic Mode Analysis, *IEEE Trans. Antennas Propag.* 70 (2) (2022) 846–855.
- [36] W. Hu, et al., Wideband Back-Cover Antenna Design Using Dual Characteristic Modes With High Isolation for 5G MIMO Smartphone, *IEEE Trans. Antennas Propag.* 70 (7) (2022) 5254–5265.
- [37] T. Li, Z.N. Chen, Wideband Sidelobe-Level Reduced Ka-Band Metasurface Antenna Array Fed by Substrate-Integrated Gap Waveguide Using Characteristic Mode Analysis, *IEEE Trans. Antennas Propag.* 68 (3) (2020) 1356–1365.
- [38] K.S. Rao, et al., Design and simulation of fixed-fixed flexure type RF MEMS switch for reconfigurable antenna, *Microsyst. Technol.* 27 (2) (2018) 455–462.
- [39] B.A. Cetiner, G.R. Crusats, L. Jofre, N. Biyikli, RF MEMS Integrated Frequency Reconfigurable Annular Slot Antenna, *IEEE Trans. Antennas Propag.* 58 (3) (2010) 626–632.
- [40] G. Liu, H. Zhang, L. Zeng, T. Huang, A polarization reconfigurable omnidirectional antenna realized by the gravity field tailored, *Int. J. RF Microw. Comput. Aided Eng.* 29 (6) (2019) e21707.
- [41] H.Y. Kang, H.Y. Hu, B.G. Han, H. Su, A reconfigurable solid-state plasma dipole antenna based on SPiN diodes, *Microelectron. Eng.* 214 (2019) 55–59.
- [42] D.-J. Kim, et al., A frequency reconfigurable dipole antenna with solid-state plasma in silicon, *Sci. Rep.* 8 (1) (2018) 14996.
- [43] Y.-P. Li, H.-F. Zhang, T. Yang, T.-Y. Sun, L. Zeng, A Multifunctional Polarization Converter Base on the Solid-State Plasma Metasurface, *IEEE J. Quantum Electron.* 56 (2) (2020) 1–7.
- [44] H. Su, H. Hu, B. Shu, B. Wang, W. Wang, J. Wang, Research of the SPiN diodes for silicon-based reconfigurable holographic antenna, *Solid State Electron.* 146 (2018) 28–33.
- [45] C.I. Liao, P.W. Sze, M.P. Houn, et al., Very High Selective Etching of GaAs/Al_{0.2}Ga_{0.8} As for Gate Recess Process to Pseudomorphic High Electron Mobility Transistors (PFETM) Applications Using Citric Buffer Solution, *Jpn. J. Appl. Phys.* 43 (6B) (2004) L800.
- [46] X.-K. Kong, J.-J. Mo, Z.-Y. Yu, W. Shi, H.-M. Li, B.-R. Bian, Reconfigurable designs for electromagnetically induced transparency in solid state plasma metamaterials with multiple transmission windows, *Int. J. Mod. Phys. B* 30 (14) (2016) 1650070.
- [47] D.-J. Kim, et al., Reconfigurable Yagi-Uda antenna based on a silicon reflector with a solid-state plasma, *Sci. Rep.* 7 (1) (2017) 17232.
- [48] L. Shen, X. Chen, T.-J. Yang, Terahertz surface plasmon polaritons on periodically corrugated metal surfaces, *Opt. Express* 16 (5) (2008) 3326–3333.
- [49] H.-F. Zhang, H. Zhang, Y. Yao, J. Yang, J.-X. Liu, A Band Enhanced Plasma Metamaterial Absorber Based on Triangular Ring-Shaped Resonators, *IEEE Photonics J.* 10 (4) (2018) 1–10.
- [50] R. Martens and D. Manteuffel, A feed network for the selective excitation of specific characteristic modes on small terminals, European Conference on Antennas and Propagation (EUCAP). 2012;1842–1846.